ARTICLES

Journal of Semiconductors
(2023) 44, 042101
doi: 10.1088/1674-4926/44/4/042101

A family of flexible two-dimensional semiconductors: $MgMX_2Y_6$ (M = Ti/Zr/Hf; X = Si/Ge; Y = S/Se/Te)

Junhui Yuan[1], Kanhao Xue[1, 2, †], Xiangshui Miao[1, 2], and Lei Ye[1, 2, †]

[1]School of Integrated Circuits, School of Optical and Electronic Information, Huazhong University of Science and Technology, Wuhan 430074, China

[2]Hubei Yangtze Memory Laboratories, Wuhan 430205, China

Abstract: Inspired by the recently predicted 2D MX_2Y_6 (M = metal element; X = Si/Ge/Sn; Y = S/Se/Te), we explore the possible applications of alkaline earth metal (using magnesium as example) in this family based on the idea of element replacement and valence electron balance. Herein, we report a new family of 2D quaternary compounds, namely $MgMX_2Y_6$ (M = Ti/Zr/Hf; X = Si/Ge; Y = S/Se/Te) monolayers, with superior kinetic, thermodynamic and mechanical stability. In addition, our results indicate that $MgMX_2Y_6$ monolayers are all indirect band gap semiconductors with band gap values ranging from 0.870 to 2.500 eV. Moreover, the band edges and optical properties of 2D $MgMX_2Y_6$ are suitable for constructing multifunctional optoelectronic devices. Furthermore, for comparison, the mechanical, electronic and optical properties of $In_2X_2Y_6$ monolayers have been discussed in detail. The success of introducing Mg into the 2D MX_2Y_6 family indicates that more potential materials, such as Ca- and Sr-based 2D MX_2Y_6 monolayers, may be discovered in the future. Therefore, this work not only broadens the existing family of 2D semiconductors, but it also provides beneficial results for the future.

Key words: two-dimensional materials; $MgMX_2Y_6$ monolayer; $In_2X_2Y_6$ monolayer; semiconductor; first-principles calculations

Citation: J H Yuan, K H Xue, X S Miao, and L Ye, A family of flexible two-dimensional semiconductors: $MgMX_2Y_6$ (M = Ti/Zr/Hf; X = Si/Ge; Y = S/Se/Te)[J]. *J. Semicond.*, 2023, 44(4), 042101. https://doi.org/10.1088/1674-4926/44/4/042101

1. Introduction

Since the discovery of graphene in 2004[1], two-dimensional (2D) materials have undergone tremendous development in these two decades[2]. Numerous families of 2D materials have been discovered experimentally or theoretically, such as group-III/IV/V/VI single-element 2D monolayers[3–7], transition metal dichalcogenides (TMDCs)[8, 9], MXenes[10], MA_2Z_4 (M = elements of transition-metal groups IVB/VB/VIB; A = Si/Ge; and Z = N/P/As)[11], α-III_2VI_3 (III = Al/Ga/In; VI = S/Se/Te)[12], and so forth. Meanwhile, 2D materials hold great potential in the fields of electronics, photoelectronics, catalysis and sensing[13–16]. Thus, the exploration of novel 2D materials is a popular topic of research.

Generally, there are three main ways to predict new 2D materials. The first is based on the existing bulk materials, which may obtain stable 2D monolayers by mechanical or liquid exfoliation, such as graphene[1], MoS_2[17] and phosphorene[18]. The second is based on crystal prediction software, such as CALYPSO[19] and UPSEX[20]. It sets appropriate structural prediction conditions and then obtains the stable structure in specified conditions. The last one is based on the existing 2D structures. The new structure is predicted by the principle of element replacement or valence electron matching, such as binary V-V compound[21].

Recently, a new family of 2D materials, i.e., $M_2X_2Y_6$ (M = metal elements; X = Si/Ge/Sn; Y = O/S/Se/Te)[22–24] or $M_IM_{II}Ge_2Y_6$ (M_I and M_{II} = metal elements, Y = S/Se/Te)[25], has been widely studied due to their rich properties. For instance, among these compounds, many materials with intrinsic ferroelectric, ferroelasticity and ferromagnetic properties have been confirmed, showing great potential in 2D memory and spintronic devices. However, we found that in the current research, the metal element M mainly focus on transition metals or group IIIA/VA elements, while the alkaline earth metals are not involved. To explore whether alkaline earth metals can form stable $M_IM_{II}X_2Y_6$-like 2D materials, we designed a series of new materials that are based on the valence electron balance strategy. Take the ion compound $In_2Ge_2Te_6$[23] as an example. In the $In_2Ge_2Te_6$, each In atom loses its three valence electrons to form an In^{3+} ion, so when one of the In^{3+} ions is replaced by a M_I^{2+} ion, a M_{II}^{4+} ion is needed to replace the remaining In^{3+} ions to achieve a valence electron balance.

Based on this idea, in this report, we selected alkaline earth metal Mg as one of the metal elements. The other was selected as the group-IVB elements (Ti/Zr/Hf) to balance the valence electrons. Consequently, we predicted a new family of 2D $MgMX_2Y_6$ (M = Ti/Zr/Hf; X = Si/Ge; Y = S/Se/Te) monolayers (MLs for short) as free standing 2D semiconductors. The structural stability, electronic structures, mechanical properties, and optical properties of 2D $MgMX_2Y_6$ have been investigated through the first-principles calculations.

2. Computational methods

All of the calculations in this work are based on density functional theory (DFT)[26]. The projector augmented-wave (PAW) method[27, 28] in the Vienna *Ab initio* Simulation Package (VASP 5.4.4) was adopted[29, 30]. The valence electron configurations were: 3s for Mg, 3s and 3p for S and Si, 4s and 4p

Correspondence to: K H Xue, xkh@hust.edu.cn; L Ye, leiye@hust.edu.cn
Received 1 NOVEMBER 2022; Revised 6 DECEMBER 2022.

Table 1. Calculated lattice constant *a*/*b* (Å), bond length Mg (In)-Y/M-Y/X-X/X-Y (Å), buckling height *d* (Å), band gaps at HSE06+SOC ($E_g^{HSE+SOC}$, eV) levels, the valence band maximum (VBM, eV) and conduce band minimum (CBM, eV) at HSE06+SOC level.

Material	*a*/*b*	Mg/In-Y	M-Y	X-X	X-Y	*d*	VBM	CBM	$E_g^{HSE+SOC}$
$MgTiSi_2S_6$	6.147	2.654	2.490	2.231	2.144	3.16	−6.74	−4.96	1.783
$MgTiSi_2Se_6$	6.461	2.798	2.619	2.254	2.299	3.37	−6.51	−4.82	1.691
$MgTiSi_2Te_6$	7.015	3.026	2.825	2.295	2.530	3.63	−5.56	−4.55	1.011
$MgTiGe_2S_6$	6.269	2.653	2.487	2.355	2.257	3.15	−6.61	−4.96	1.654
$MgTiGe_2Se_6$	6.572	2.798	2.620	2.385	2.401	3.37	−6.36	−4.84	1.517
$MgTiGe_2Te_6$	7.107	3.026	2.825	2.435	2.617	3.64	−5.47	−4.60	0.870
$MgZrSi_2S_6$	6.250	2.681	2.607	2.233	2.149	3.26	−6.83	−4.53	2.307
$MgZrSi_2Se_6$	6.556	2.820	2.739	2.261	2.302	3.48	−6.71	−4.49	2.225
$MgZrSi_2Te_6$	7.102	3.045	2.947	2.303	2.530	3.74	−5.69	−4.38	1.314
$MgZrGe_2S_{-6}$	6.372	2.678	2.608	2.354	2.261	3.26	−6.78	−4.69	2.084
$MgZrGe_2Se_6$	6.662	2.818	2.740	2.388	2.402	3.49	−6.48	−4.58	1.905
$MgZrGe_2Te_6$	7.187	3.042	2.946	2.440	2.616	3.76	−5.52	−4.44	1.074
$MgHfSi_2S_6$	6.218	2.675	2.580	2.228	2.151	3.25	−6.92	−4.42	2.500
$MgHfSi_2Se_6$	6.530	2.815	2.711	2.256	2.303	3.46	−6.69	−4.30	2.398
$MgHfSi_2Te_6$	7.084	3.041	2.919	2.300	2.532	3.72	−5.64	−4.18	1.456
$MgHfGe_2S_6$	6.341	2.674	2.580	2.348	2.262	3.25	−6.83	−4.60	2.232
$MgHfGe_2Se_6$	6.638	2.815	2.711	2.383	2.404	3.46	−6.47	−4.43	2.045
$MgHfGe_2Te_6$	7.172	3.041	2.917	2.436	2.618	3.73	−5.58	−4.39	1.189
$In_2Si_2S_6$	6.278	2.706	–	2.270	2.150	3.41	−6.92	−4.21	2.704
$In_2Si_2Se_6$	6.600	2.835	–	2.294	2.303	3.59	−6.44	−4.25	2.185
$In_2Si_2Te_6$	7.153	3.044	–	2.329	2.533	3.83	−5.54	−4.28	1.261
$In_2Ge_2S_6$	6.385	2.708	–	2.375	2.259	3.43	−6.93	−4.47	2.459
$In_2Ge_2Se_6$	6.696	2.836	–	2.409	2.401	3.61	−6.44	−4.49	1.952
$In_2Ge_2Te_6$	7.234	3.043	–	2.457	2.616	3.85	−5.48	−4.26	1.220

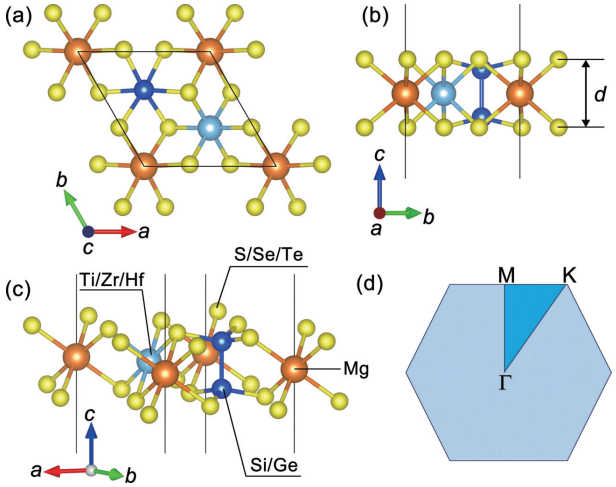

Fig. 1. (Color online) (a) The top view and (b, c) side view of monolayer $MgMX_2Y_6$. (d) The corresponding first Brillouin zone of $MgMX_2Y_6$ monolayers.

for Se and Ge, 5s and 5p for Te and In, 4s and 4d for Ti, 4s, 4p, 5s and 4d for Zr, 6s and 5d for Hf. An energy cutoff of 500 eV with a 9 × 9 × 1 Γ-centered k-mesh was used for the plane wave basis. For the exchange-correlation energy, the Perdew-Burke-Ernzerhof (PBE) functional[31] formal within generalized gradient approximation (GGA)[31] was implemented. Due to the band gap underestimation problem in GGA[32, 33], the Heyd-Scuseria-Ernzerhof (HSE06) hybrid functional was further employed in electronic band structure calculations[34]. In addition, the spin-orbit coupling (SOC) effect has been further considered in the electronic band calculations. In structural optimization, a strict 1 meV/Å force criterion and 10^{-7} eV energy criterion were used, respectively. Furthermore, a 20 Å vacuum layer was introduced in all 2D monolayers to avoid interactions with adjacent layers. Phonon dispersions of 2D $MgMX_2Y_6$ were calculated by the density functional perturbation theory (DFPT) using PHONOPY code[35]. The *ab initio* molecular dynamics (AIMD) simulations were further performed with a 3 × 3 × 1 (90 atoms in total) supercell for 5 ps at 300 K.

3. Results and discussion

3.1. Structure and stability

We start with the crystal structure of 2D $MgMX_2Y_6$ (M = Ti/Zr/Hf; X = Si/Ge; Y = S/Se/Te), as shown in Fig. 1. The ML $MgMX_2Y_6$ possess a hexagonal symmetry with the space group of $P31_2$ (No. 149). In ML $MgMX_2Y_6$, there are five atomic layers, in the order of Y-X-Mg/M-X-Y, while the Mg and M atoms are strictly in the same plane. In addition, there is a X-X dimer in the 2D $MgMX_2Y_6$, which is similar to that of P-P dimer in 2D ABP_2Y_6 (A = Cu/Zn/Ge/Ag/Cd, B = Ga/In/Bi, Y = S/Se)[36]. We have summarized the optimized lattice constant *a*/*b*, bond length Mg-Y/M-Y/X-X/X-Y and buckling height *d* of $MgMX_2Y_6$ MLs in Table 1. As shown in Table 1, the lattice constants, bond lengths and buckling heights of $MgMX_2Y_6$ MLs all vary periodically. For example, in $MgTiSi_2Y_6$ MLs, the lattice constants and buckling heights are 6.147/6.461/7.015 Å and 3.16/3.37/3.63 Å for $MgTiSi_2S_6$/$MgTiSi_2Se_6$/$MgTiSi_2Te_6$, respectively. In addition, for comparison, we have also given the calculated results of $In_2X_2Y_6$ MLs, as summarized in Table 1. The lattice constants, bond lengths and buckling heights of $In_2X_2Y_6$ MLs are vary periodically and are close to that of $MgHfX_2Y_6$ MLs.

The structural stability is a vital criterion to evaluate whether the newly predicted 2D materials can be applied in electron-

Fig. 2. (Color online) Phonon dispersion of ML $MgMX_2Y_6$ and $In_2X_2Y_6$.

ic devices. For the newly predicted 2D $MgMX_2Y_6$ MLs, the first concern is their kinetic stability. To evaluate the kinetic stability, we calculated the phonon dispersions of these 18 monolayers. As shown in Fig. 2, all the predicted $MgMX_2Y_6$ MLs exhibit superior kinetic stability due to the free of imaginary frequency in phonon dispersions. In addition, although some phonon dispersions of $In_2X_2Y_6$ MLs exhibit tiny imaginary frequency near the Γ point which is caused by the computational error, the kinetic stability of $In_2X_2Y_6$ MLs are also been confirmed. Subsequently, we examined the thermodynamic stability of $MgMX_2Y_6$ MLs based on the AIMD simulations. During the simulations, the temperature is kept at 300 K for a time scale of 5 ps. The total energy fluctuations of $MgMX_2Y_6$ MLs are presented in Fig. 3. The corresponding crystal structures of $MgMX_2Y_6$ MLs after the simulation are also inserted in Fig. 3. No obvious structural reconstruction has been found after the simulation and the total energy fluctuations are tiny, indicating the high thermodynamic stability of these monolay-

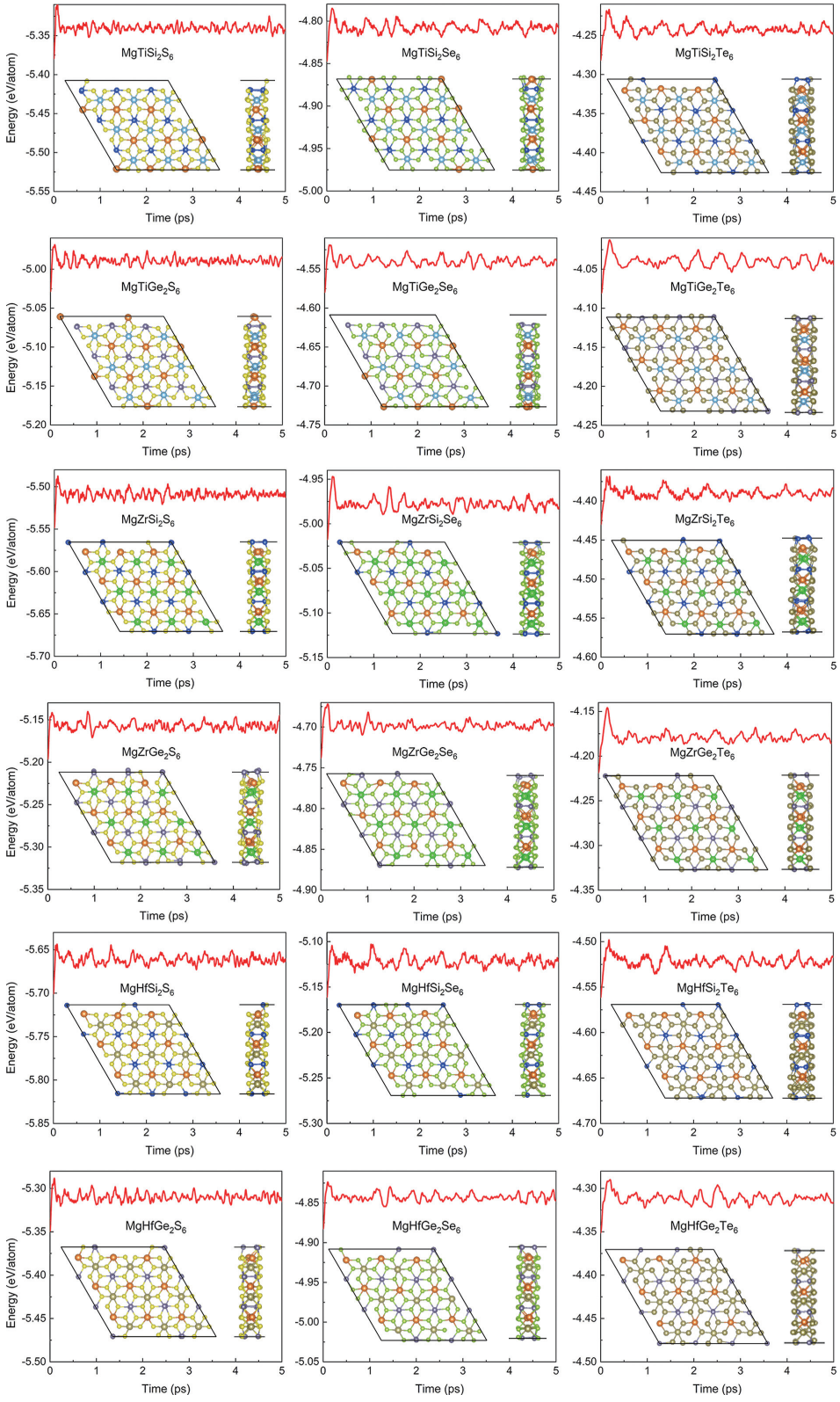

Fig. 3. (Color online) AIMD simulation results of $MgMX_2Y_6$ MLs at 300 K.

ers at room temperature.

Furthermore, cohesive energy (E_{coh}) is an important factor to judge the thermal stability. The E_{coh} of $MgMX_2Y_6$ MLs is defined as $E_{coh} = (E_{Mg} + E_M + 2E_X + 6E_Y - E_{MgMX_2Y_6})/10$, where the $E_{Mg}/E_M/E_X/E_Y$ and $E_{MgMX_2Y_6}$ represent the energy of single Mg/M/X/Y atom and the total energy of $MgMX_2Y_6$ MLs, respectively. According to the definition, larger positive value of E_{coh} indicate higher thermal stability. The calculated cohesive energies of $MgMX_2Y_6$ MLs are shown in Fig. 4. In addition, for comparison, the cohesive energies of $In_2X_2Y_6$ MLs and three typical 2D materials (buckled arsenene, phosphorene and silicene) have also been given. The calculated cohesive energies of the predicted 18 monolayers are ranging from 3.310 eV/atom ($MgTiGe_2Te_6$) to 4.670 eV/atom ($MgHfSi_2S_6$). For the $In_2X_2Y_6$ MLs, the calculated cohesive energies (see Fig. 4) MLs are ranging from 4.033 eV/atom ($In_2Ge_2Te_6$) to

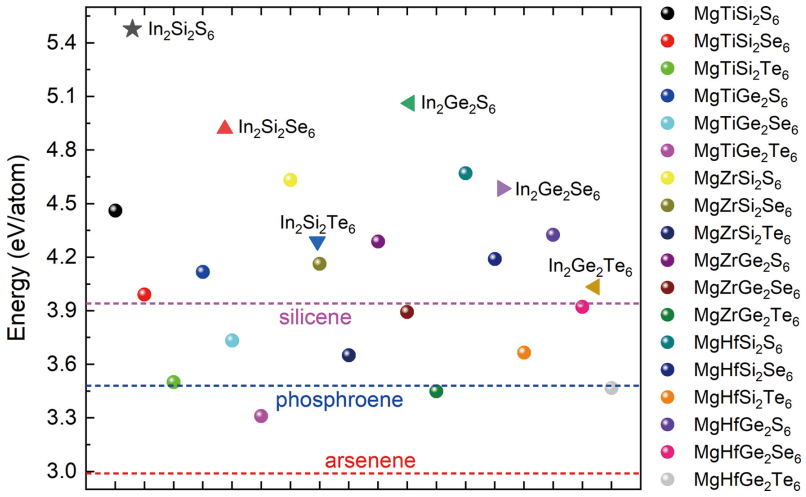

Fig. 4. (Color online) Calculated cohesive energies of $MgMX_2Y_6$ and $In_2X_2Y_6$ MLs.

5.478 eV/atom ($In_2Si_2S_6$), which is superior to that of most of the $MgMX_2Y_6$ MLs. Obviously, the calculated cohesive energies of $MgMX_2Y_6$ are comparable or superior to that of buckled arsenene (2.989 eV/atom)[37], phosphorene (3.44 eV/atom)[38] and silicene (3.94 eV/atom)[39]. Since these three 2D materials have been realized experimentally, the predicted 2D $MgMX_2Y_6$ in this work may also possess high experimental feasibility.

We also checked the mechanical stability of $MgMX_2Y_6$ and $In_2X_2Y_6$ MLs. To verify the mechanical stability, the independent elastic constants of $MgMX_2Y_6$ and $In_2X_2Y_6$ MLs have been calculated and the results are summarized in Table 2. For a stable 2D material, it is required to meet the Born-Huang criterion[40], i.e., $C_{11}C_{22} - C_{12}^2 > 0$, $C_{66} > 0$. Since ML $MgMX_2Y_6$ and $In_2X_2Y_6$ possess a hexagonal symmetry, there are $C_{11} = C_{22}$. Therefore, for 2D $MgMX_2Y_6$ and $In_2X_2Y_6$, it needs to be satisfied $C_{11}^2 - C_{12}^2 > 0$, $C_{66} > 0$. As shown in Table 2, all of the monolayers satisfy the Born-Huang criteria and exhibit high mechanical stability. These results indicate that $MgMX_2Y_6$ MLs possess high kinetic, thermal and mechanical stabilities, and might be realized experimentally in the future.

To further confirm our strategy of achieving valence electron balance based on element substitution, we present the results of Bader charge analysis[41] for $MgMX_2Y_6$ and $In_2X_2Y_6$, as summarized in Table 3. The results show that in $MgMX_2Y_6$ and $In_2X_2Y_6$ MLs, both Mg and In atoms lose all of their valence electrons and exhibit strong metallic properties. The Bader charge distribution of similar or identical elements in $MgMX_2Y_6$ and $In_2X_2Y_6$ is almost the same. Taking the ML $In_2Si_2S_6$ and $MgHfSi_2S_6$ as examples, the Bader charge analysis shows that Si loses 2.98 e and 3.00 e in $MgHfSi_2S_6$ and $In_2Si_2S_6$, respectively. While for that of S, it gains 1.99 e and 2.00 e for $MgHfSi_2S_6$ and $In_2Si_2S_6$, respectively. Meanwhile, the Mg and Hf lose 2 e and 3.98 e respectively, which is very close to the total amount of electrons lose by two In atoms (6 e). Thus, the corresponding elements in $MgHfSi_2S_6$ and $In_2Si_2S_6$ lose or gain almost the same amount of charge. The Bader charge analysis results well proved the valence electron balance strategy. For $MgTiX_2Y_6$ and $MgZrX_2Y_6$ MLs, although the Bader charge analysis results are somewhat different from those of $MgHfX_2Y_6$, they are mainly caused by the differences between Ti, Zr and Hf elements, which does not affect the reasonable prediction of the family of $MgMX_2Y_6$.

3.2. Mechanical properties

Young's modulus and Poisson's ratio are important indicators to characterize the mechanical properties of materials. According to the crystal symmetry, the Young's modulus and Poisson's ratio of $MgMX_2Y_6$ and $In_2X_2Y_6$ MLs should be isotropic. Therefore, the corresponding axial Young's modulus (Y_{11}/Y_{22}, the θ is set to 0°/180° and 90°/270°) and Poisson's ratio (v_{11}/v_{22}) can be calculated by simplified formulas, as follow:

$$Y_{11} = Y_{22} = \frac{C_{11}^2 - C_{12}^2}{C_{11}}, \tag{1}$$

$$v_{11} = v_{22} = \frac{C_{12}}{C_{11}}. \tag{2}$$

We have given the independent elastic constants in Table 2. The calculated axial Young's modulus and Poisson's ratio of $MgMX_2Y_6$ MLs are also listed in Table 2. The Young's moduli of $MgMX_2Y_6$ MLs range from 37.52 N/m ($MgZrGe_2Te_6$ and $MgHfGe_2Te_6$) to 67.19 N/m ($MgHfSi_2S_6$). For $In_2X_2Y_6$ MLs, the Young's moduli range from 42.80 N/m ($In_2Ge_2Te_6$) to 66.55 N/m ($In_2Si_2S_6$), which is comparable to that of $MgMX_2Y_6$ MLs. Compared to some other 2D materials, such as graphene (342.2 N/m)[42], BN (275.8 N/m)[43] and MoS_2 (197.9 N/m)[3], the $MgMX_2Y_6$ MLs possess much lower stiffness and hold great potential in flexible electronic devices. In addition, the Young's moduli of $MgMX_2Y_6$ MLs also show a cyclical trend. For instance, the Young's moduli of $MgZrSi_2S_6$, $MgZrSi_2Se_6$ and $MgZrSi_2Te_6$ are 60.23, 51.52 and 40.09 N/m, respectively, showing a decreasing trend when Y goes from S to Te. This can be explained by the electronegativity. Since 2D $MgMX_2Y_6$ is dominated by the ionic bond, its bond strength mainly depends on the number of electrons gained and lost in the bonding process. The electronegativity values of S, Se and Te are 2.59, 2.42 and 2.16, respectively. Therefore, in the bonding process, the sulfur-containing system has a stronger ionic bond, and the material possesses larger stiffness. Compared with the periodic change of Young's modulus, the Poisson's ratio of $MgMX_2Y_6$ and $In_2X_2Y_6$ MLs is relatively stable. The Poisson's ratios of $MgMX_2Y_6$ and $In_2X_2Y_6$ MLs are around 0.27–0.30 and 0.30–0.31, respectively, larger than that of graphene (0.173)[42] and BN (0.22)[43]. The relatively close Poisson's ratio

Table 2. Calculated elastic constant $C_{11}/C_{22}/C_{12}/C_{66}$ (N/m), axial Young's modulus Y_{11}/Y_{22} (N/m), Poisson's ratio v_{11}/v_{22}, ultimate strength σ* (N/m), ultimate strain ε^*, corresponding to the ultimate strength for *x*, *y*, and biaxial tensions of $MgMX_2Y_6$ and $In_2X_2Y_6$ MLs.

Material	C_{11}/C_{22}	C_{12}	C_{66}	$C_{11}^2 - C_{12}^2$	Y_{11}/Y_{22}	v_{11}/v_{22}	*x*		*y*		Biaxial	
							σ^*	ε^*	σ^*	ε^*	σ^*	ε^*
$MgTiSi_2S_6$	71.88	20.35	25.76	4752.31	66.12	0.28	5.67	0.14	4.77	0.11	8.95	0.17
$MgTiSi_2Se_6$	59.69	17.27	21.21	3264.25	54.69	0.29	4.93	0.16	3.70	0.10	6.23	0.12
$MgTiSi_2Te_6$	45.56	13.51	16.03	1893.41	41.56	0.30	4.16	0.20	2.53	0.08	4.83	0.12
$MgTiGe_2S_6$	66.55	19.82	23.36	4036.08	60.65	0.30	5.46	0.15	3.85	0.08	6.92	0.12
$MgTiGe_2Se_6$	55.27	16.54	19.37	2781.04	50.32	0.30	4.63	0.18	3.32	0.10	6.07	0.14
$MgTiGe_2Te_6$	41.09	11.18	14.95	1563.48	38.05	0.27	3.78	0.22	2.29	0.08	4.51	0.14
$MgZrSi_2S_6$	65.28	18.17	23.56	3932.06	60.23	0.28	5.83	0.17	3.76	0.10	6.90	0.12
$MgZrSi_2Se_6$	55.89	15.63	20.13	2879.43	51.52	0.28	5.08	0.19	3.13	0.09	5.70	0.11
$MgZrSi_2Te_6$	43.58	12.34	15.62	1746.97	40.09	0.28	4.23	0.23	2.33	0.08	4.38	0.11
$MgZrGe_2S_6$	60.66	17.36	21.65	3378.06	55.69	0.29	5.50	0.17	6.53	0.12	6.53	0.12
$MgZrGe_2Se_6$	51.80	14.83	18.49	2463.40	47.56	0.29	4.74	0.20	2.90	0.09	5.38	0.12
$MgZrGe_2Te_6$	40.76	11.50	14.63	1529.26	37.52	0.28	3.87	0.25	2.14	0.08	4.44	0.15
$MgHfSi_2S_6$	73.04	20.68	26.18	4907.98	67.19	0.28	6.42	0.17	4.47	0.12	7.53	0.11
$MgHfSi_2Se_6$	60.66	17.55	21.55	3371.17	55.58	0.29	5.98	0.11	3.63	0.10	5.54	0.19
$MgHfSi_2Te_6$	45.56	13.51	16.03	1893.41	41.56	0.30	4.56	0.22	2.52	0.09	4.63	0.11
$MgHfGe_2S_6$	60.66	17.36	21.65	3378.06	55.69	0.29	6.04	0.18	4.09	0.10	6.07	0.10
$MgHfGe_2Se_6$	51.80	14.83	18.49	2463.40	47.56	0.29	5.14	0.20	3.27	0.09	5.66	0.12
$MgHfGe_2Te_6$	40.76	11.50	14.63	1529.26	37.52	0.28	4.13	0.23	2.34	0.08	4.49	0.13
$In_2Si_2S_6$	73.27	22.19	25.54	4876.27	66.55	0.30	4.35	0.11	4.17	0.11	6.89	0.14
$In_2Si_2Se_6$	62.45	19.03	21.71	3537.50	56.65	0.30	3.78	0.11	3.28	0.11	5.81	0.14
In_2Si_2Te	50.16	14.99	17.59	2291.59	45.69	0.30	3.05	0.11	2.20	0.09	4.63	0.13
$In_2Ge_2S_6$	68.56	21.01	23.77	4258.46	62.11	0.31	4.22	0.10	4.02	0.12	6.97	0.15
$In_2Ge_2Se_6$	58.56	18.09	20.23	3101.50	52.96	0.31	3.70	0.11	3.17	0.11	6.04	0.15
$In_2Ge_2Te_6$	47.12	14.28	16.42	2016.88	42.80	0.30	3.03	0.12	2.10	0.09	4.61	0.14

Table 3. Bader charge analysis of $MgMX_2Y_6$ and $In_2X_2Y_6$ MLs.

Material	Mg/In	Ti/Zr/Hf	Si/Ge	S/Se/Te	Material	Mg/In	Ti/Zr/Hf	Si/Ge	S/Se/Te
$MgTiSi_2S_6$	+2	+1.96	+3.00	−1.66	$MgHfSi_2S_6$	+2	+3.98	+2.98	−1.99
$MgTiSi_2Se_6$	+2	+2.04	+2.96	−1.66	$MgHfSi_2Se_6$	+2	+3.76	+2.94	−1.94
$MgTiSi_2Te_6$	+2	+1.98	+0.65	−0.88	$MgHfSi_2Te_6$	+2	+2.88	+0.74	−1.06
$MgTiGe_2S_6$	+2	+1.98	+3.02	−1.67	$MgHfGe_2S_6$	+2	+3.98	+2.98	−1.99
$MgTiGe_2Se_6$	+2	+1.72	+2.97	−1.61	$MgHfGe_2Se_6$	+2	+3.96	+2.96	−1.98
$MgTiGe_2Te_6$	+2	+1.58	+0.46	−0.75	$MgHfGe_2Te_6$	+2	+2.88	+0.50	−0.98
$MgZrSi_2S_6$	+2	+2.24	+2.98	−1.70	$In_2Si_2S_6$	+3	–	+3.00	−2.00
$MgZrSi_2Se_6$	+2	+2.06	+2.95	−1.66	$In_2Si_2Se_6$	+3	–	+2.97	−1.99
$MgZrSi_2Te_6$	+2	+1.78	+0.75	−0.88	$In_2Si_2Te_6$	+3	–	+0.54	−1.18
$MgZrGe_2S_6$	+2	+2.24	+2.98	−1.70	$In_2Ge_2S_6$	+3	–	+2.97	−1.99
$MgZrGe_2Se_6$	+2	+2.06	+2.95	−1.66	$In_2Ge_2Se_6$	+3	–	+2.97	−1.99
$MgZrGe_2Te_6$	+2	+1.84	+0.51	−0.81	$In_2Ge_2Te_6$	+3	–	+0.48	−1.16

indicates that 2D $MgMX_2Y_6$ and $In_2X_2Y_6$ possess similar response to tensile or compressive stresses in the plane.

To further evaluate the mechanical properties, the strain-stress relationships of $MgMX_2Y_6$ and $In_2X_2Y_6$ MLs have been plotted in Fig. 5 and the details are summarized in Table 2. As shown in Fig. 5 and Table 2, the ultimate strains (ε^*) of $MgMX_2Y_6$ MLs along the *x*-direction are ranging from 0.11 ($MgHfSi_2Se_6$) to 0.25 ($MgZrGe_2Te_6$), much superior to that of $In_2X_2Y_6$ MLs (around 0.10 to 0.12) and lower than that of ML MX_2 (M = Mo, W; X = Se, Se, Te) (0.28–0.32)[44]. The corresponding ultimate strengths (σ^*) of $MgMX_2Y_6$ MLs are about 3.78 N/m ($MgTiGe_2Te_6$)–6.42 N/m ($MgHfSi_2S_6$), still larger than that of most of $In_2X_2Y_6$ MLs (3.03–4.35 N/m). For the tensile strain along the *y*-direction, the ultimate strains of $MgMX_2Y_6$ MLs are much smaller than that of *x*-direction, just about 0.08 to 0.12, which is comparable to that of $In_2X_2Y_6$ MLs (0.09–0.12). In addition, both the ultimate strength of $MgMX_2Y_6$ (2.14–6.53 N/m) and $In_2X_2Y_6$ (2.10–4.17 N/m) MLs along the *y*-direction are smaller than that of *x*-direction under the same strain. When undergoing biaxial strain, the ultimate strain of $In_2X_2Y_6$ MLs is very close to each other (0.13–0.15), while $MgMX_2Y_6$ MLs shows a relatively large difference (0.10–0.19). The ultimate strength of $MgMX_2Y_6$ MLs with biaxial strain is around 4.38–8.95 N/m, while for that of $In_2X_2Y_6$ MLs is about 4.61–6.97 N/m. Generally, the mechanical properties of the $MgMX_2Y_6$ MLs are comparable to or better than the $In_2X_2Y_6$ MLs.

3.3. Electronic structure

The electronic properties of 2D materials are important

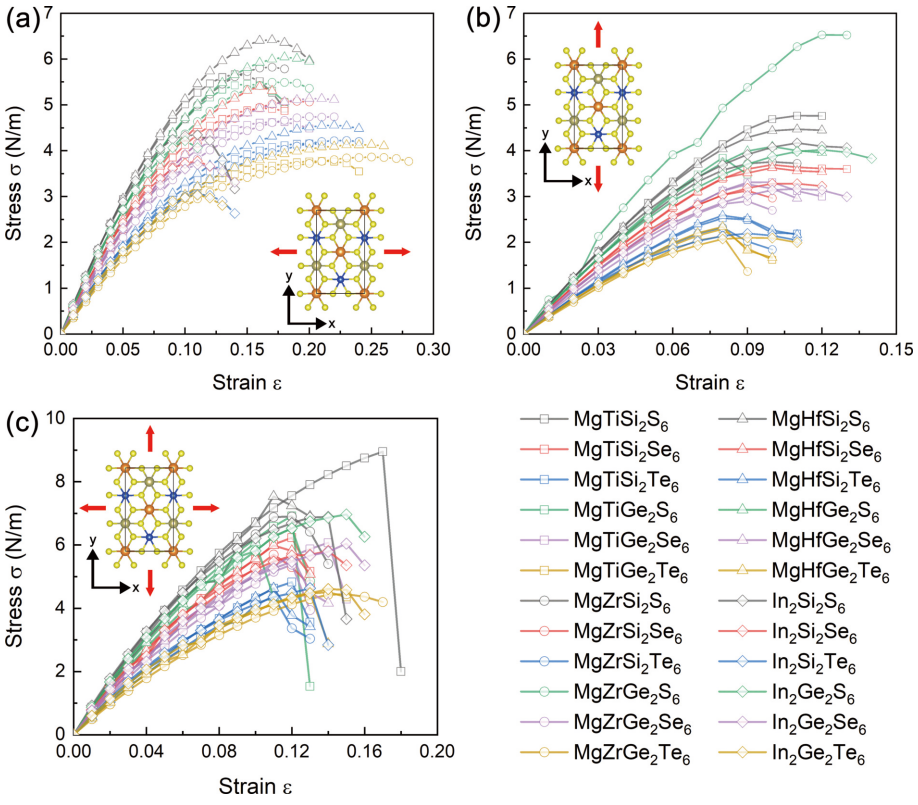

Fig. 5. (Color online) Tensile stress σ, as a function of uniaxial strain, ε, along the (a) x- and (b) y-directions and (c) of biaxial strain, respectively, for ML $MgMX_2Y_6$ and $In_2X_2Y_6$.

for their application in nanoelectronics. On the one hand, the GGA-PBE always underestimate the band gaps of semiconductors; while on the other hand, spin-orbit coupling (SOC) effect will strongly affect the band structures of compounds with heavier element, such as Si, Ge, Se and Te. Therefore, we have given the band gaps and band structures of $MgMX_2Y_6$ and $In_2X_2Y_6$ MLs based on hybrid functional HSE06 within SOC effect involved. The band gaps ($E_g^{HSE+SOC}$) are summarized in Table 1, while the projected electronic band structures of $MgMX_2Y_6$ and $In_2X_2Y_6$ MLs are shown in Fig. 6 and Fig. 7, respectively. All the $MgMX_2Y_6$ MLs are indirect band gap semiconductors with the band gap values ranging from 0.870 eV ($MgTiGe_2Te_6$) to 2.500 eV ($MgHfSi_2S_6$). Such a wide range of band gaps in $MgMX_2Y_6$ MLs enable the selection of suitable monolayers for different requirements. For $In_2X_2Y_6$ MLs, the band gaps are ranging from 1.220 ($In_2Ge_2Te_6$) to 2.704 eV ($In_2Si_2S_6$). In contrast from the $MgMX_2Y_6$ MLs, which all exhibit indirect band gap features, the $In_2Ge_2Se_6$ and $In_2Ge_2Te_6$ of $In_2X_2Y_6$ MLs are direct band gap semiconductors with the VBM and CBM both located at Γ point. The direct band gap features of $In_2Ge_2Se_6$ and $In_2Ge_2Te_6$ may more favorable for photoelectric device applications[23, 45].

Although the $MgMX_2Y_6$ MLs are all indirect band gap semiconductors, their morphology of band structures still shows many differences. The morphology of band structures can be divided into three types according to the Y element. For the $MgMX_2S_6$ MLs, the VBMs are located along the Γ–K direction and closer to K. While for the $MgMX_2Se_6$ MLs, the VBMs are either located along the Γ–K direction and closer to K point or at Γ point, and the energy differences between these two points are merely several or dozens of meV. For example, the VBM of ML $MgZrGe_2Se_6$ is located along the Γ–K direction and closer to K point and the energy difference between the VBM and Γ point is only 28 meV. However, the VBM of ML $MgHfGe_2Se_6$ is just located at Γ point and the energy difference for these two points is merely 6 meV. The last one is $MgMX_2Te_6$, whose VBMs are all located at the Γ point. For the conduction bands, their morphological change trend is roughly the same, and their CBMs are mainly located at the M point or close to the K point. Furthermore, the band gap values of $MgMX_2Y_6$ MLs also show a periodic change trend as expected. For instance, in $MgHfGe_2Y_6$ MLs, the band gaps decreased from 2.232 to 1.189 eV when Y goes from S to Te. Turn to the $In_2X_2Y_6$ MLs, as shown in Fig. 7, the CBMs of $In_2Si_2S_6$, $In_2Si_2Se_6$ and $In_2Ge_2S_6$ are located at Γ point. The CBMs of $In_2Si_2S_6$ and $In_2Ge_2S_6$ are located at M point, in contrast from the $In_2Si_2Se_6$ with VBM located at K point. For $In_2Si_2Te_6$, the VBM is located at Γ point, while the CBM is located along the K–M direction and close to the K point. Similar to $MgMX_2Y_6$ MLs, the band gap values of $In_2X_2Y_6$ MLs also show a periodic change trend.

For the orbital contribution, as shown in Fig. 6, the conduction band of ML $MgMX_2Y_6$ is mainly contributed by the d-orbit of Ti/Zr/Hf atom, while the valence band is dominated by the p-orbit of S/Se/Te element. Similarly, for $In_2X_2Y_6$ MLs (see Fig. 7), the conduction band is mainly contributed by the p-orbit of In atom, while the valence band is dominated by the p-orbit of non-metal element. In addition, the Si/Ge-p orbit contributes to both the valence band and conduction band in $MgMX_2Y_6$ and $In_2X_2Y_6$ MLs. No contribution from Mg-s orbit is found in the range of energy scales shown in Fig. 6, mainly due to the electron loss in the bonding process of Mg, so its orbital contribution will be located at deeper energy levels.

Next, we focus on the band edges (VBM and CBM) of Mg-

Fig. 6. (Color online) Projected electronic band structures of $MgMX_2Y_6$ MLs based on HSE06+SOC calculation.

MX_2Y_6 and $In_2X_2Y_6$ MLs. At present, the application of 2D semiconductors can be divided into two aspects: the first is to make use of its intrinsic properties, the second is to make use of its heterojunction properties with other materials. Regardless of which aspect, it is necessary to study its band edge characteristics. We have shown the band edges of $MgMX_2Y_6$ and $In_2X_2Y_6$ MLs at HSE06+SOC level in Fig. 8, and the details are summarized in Table 1. The energy levels of CBMs for $MgMX_2Y_6$ MLs range from –4.96 to –4.18 eV, while for VBMs, the energy levels are around –6.92 to –5.47 eV. For $In_2X_2Y_6$

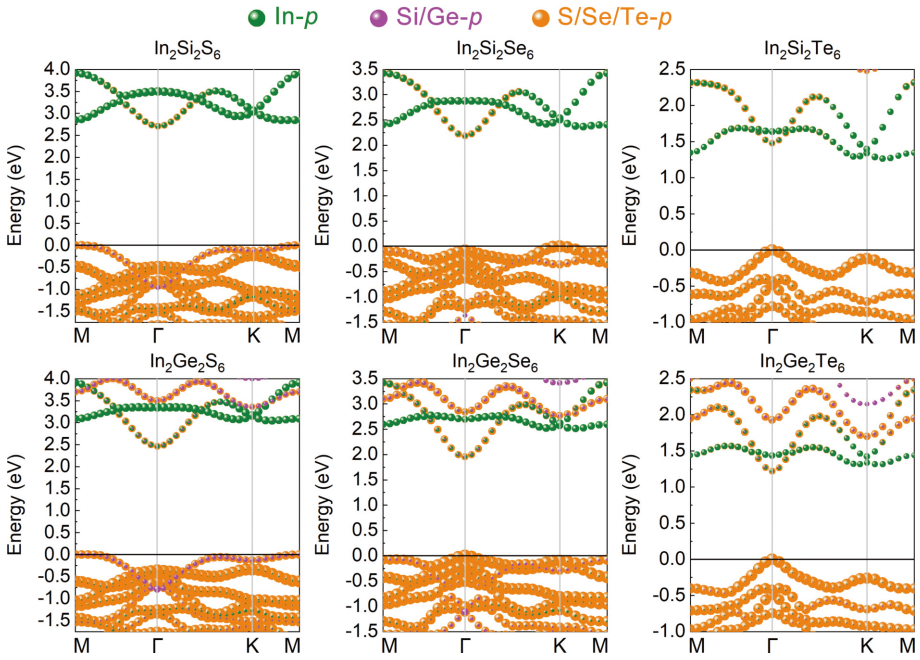

Fig. 7. (Color online) Projected electronic band structures of $In_2X_2Y_6$ MLs based on HSE06+SOC calculation.

Fig. 8. (Color online) The band edges of $MgMX_2Y_6$ and $In_2X_2Y_6$ MLs. The vacuum level is set to zero. The work functions of Ag, Ti, Cu, Au and Pt have been marked in the figure.

MLs, the energy levels of CBMs for $In_2X_2Y_6$ MLs range from –4.49 to –4.21 eV, while for VBMs, the energy levels are around –6.92 to –5.48 eV, both are comparable to that of $MgHfX_2Y_6$ MLs. The work functions of Ag, Ti, Cu, Au and Pt are 4.26, 4.33, 4.65, 5.1 and 5.65 eV, respectively. It can be seen that Schottky contact or Ohmic contact can be achieved in metal/$MgMX_2Y_6$ and metal/$In_2X_2Y_6$ heterostructure by selecting appropriate electrode or 2D materials. Meanwhile, as shown in Fig. 8, type-I (such as $MgTiGe_2Te_6/MgZrSi_2Te_6$, $In_2Si_2S_6/In_2Si_2Te_6$) and type-II (such as $MgTiSi_2Se_6/MgTiSi_2Te_6$, $In_2Ge_2Se_6/In_2Ge_2Te_6$) band alignment can also be realized by the combination of different materials in $MgMX_2Y_6$ and $In_2X_2Y_6$ MLs, which is beneficial for the realization of different types of optoelectronic devices. The wide band gaps and band edges make $MgMX_2Y_6$ and $In_2X_2Y_6$ MLs potential candidates for realizing multifunctional nanoelectronic devices.

3.4. Optical properties

Finally, the band gaps of $MgMX_2Y_6$ MLs cover a wide range (0.870–2.500 eV), so it is necessary to evaluate its light harvesting capability. We mainly focus on the absorption coefficient, which can be expressed as follows[46]: $\alpha(\omega) = \frac{\sqrt{2}\omega}{c}\{\sqrt{\varepsilon_1^2(\omega)+\varepsilon_2^2(\omega)}-\varepsilon_1(\omega)\}^{1/2}$, where ω represents the photon frequency, $\varepsilon_1(\omega)$ and $\varepsilon_2(\omega)$ are the real and imaginary part of the dielectric function, respectively. And the dielectric function was obtained by $\varepsilon(\omega) = \varepsilon_1(\omega) + i\varepsilon_2(\omega)$. The absorption coefficients of ML $MgMX_2Y_6$ and $In_2X_2Y_6$ were calculated using the independent particle approximation (IPA) at HSE+SOC level. Fig. 9 shows the absorption coefficients of $MgMX_2Y_6$ MLs. For $MgTiX_2Y_6$ and $MgZrX_2Y_6$ MLs (Figs. 9(a) and 9(b)), the absorption coefficients in near-infrared (NIR) and visible light (VIS) region are much higher than that of $MgHfX_2Y_6$ MLs (Fig. 9(c)), and can reach the order of 10^5 cm^{-1}, especially for $MgTiGe_2Te_6$ and $MgZrGe_2Te_6$. Furthermore, from the distribution of absorption peaks, it can be seen that the optical band gaps of $MgMX_2Y_6$ MLs are larger than the electronic band gap. For example, the absorption peaks of $MgHfX_2Y_6$ MLs are all located in the deep ultraviolet (UV) region (see Fig. 9(c)), while the electronic band gaps of $MgHfX_2Y_6$ MLs range from 1.189 to 2.500 eV. This is mainly due to the fact that in indirect band gap semiconductors, light absorption is accompanied by absorption or emission of phonons, which will consume a large quantity of energy. In addition, the light absorptions of $MgHfX_2Y_6$, $MgTiSi_2Se_6$ and $MgTiSi_2Te_6$ are mainly concentrated in the UV region, which indicate potential applications of UV optoelectronic devices. Meanwhile, strong optical absorption coefficients in NIR, VIS and UV light have been confirmed for $MgTiGe_2Te_6$, $MgZrSi_2Te_6$ and $MgZrGe_2Te_6$, which suggests a better potential in multifunctional optoelectronic devices. The remaining seven monolayers possess considerable optical absorption in the VIS and UV regions, and are also potential candidates for optoelectronic devices. Finally, for comparison, the optical characteristics of $In_2X_2Y_6$ MLs are also investigated, as shown in Fig. 9(d). For $In_2X_2Y_6$ MLs, the optical absorption coefficient is mainly concentrated in VIS and UV region, and can reach the order of 10^5 cm^{-1}, comparable to that of $MgZrX_2Y_6$ MLs. The suitable band gap value and direct band gap feature make $In_2Ge_2Te_6$

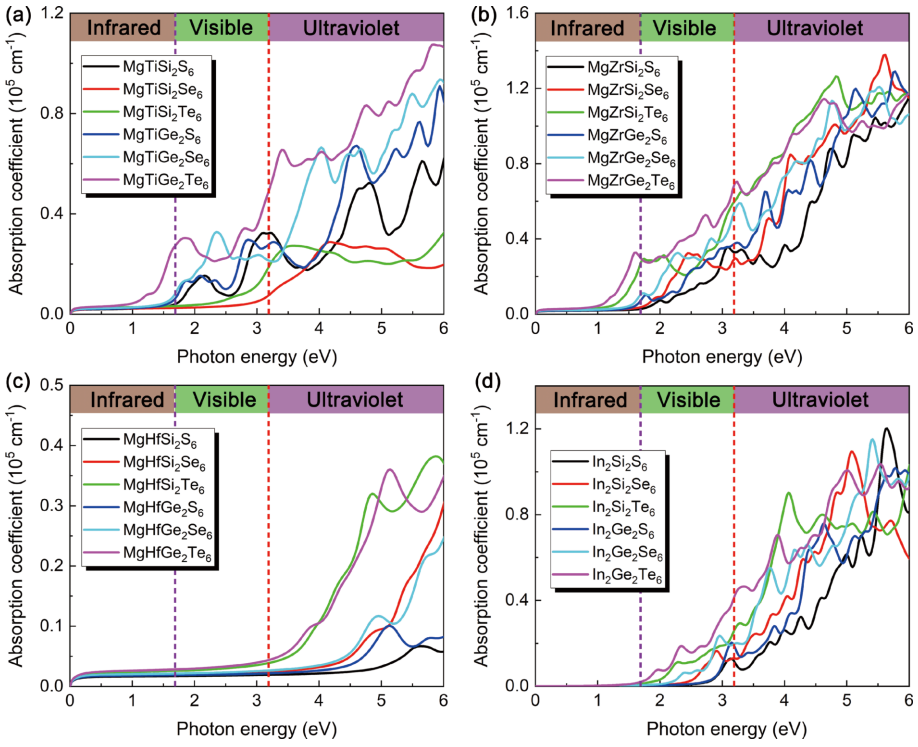

Fig. 9. (Color online) Optical absorption coefficient of $MgMX_2Y_6$ and $In_2X_2Y_6$ MLs based on HSE06+SOC calculations.

exhibit stronger visible light absorption than the rest of $In_2X_2Y_6$ MLs. The considerable optical absorption of $In_2X_2Y_6$ MLs in the VIS and UV regions suggest its potential for optoelectronic devices.

4. Conclusions

In summary, based on the valence electron balance, we have predicted a new family of 2D semiconductors; that is, $MgMX_2Y_6$ (M = Ti/Zr/Hf; X = Si/Ge; Y = S/Se/Te) MLs. The 18 newly predicted 2D monolayers have good kinetic, thermodynamic and mechanical stability. Small Young's modulus and moderate Poisson's ratio indicate that 2D $MgMX_2Y_6$ is suitable for flexible electronic devices. Electronic structure analysis shows that these monolayers are all indirect band gap semiconductors with band gap values ranging from 0.870 to 2.500 eV. In addition, its band-edge properties are suitable for constructing various types of electronic devices. Optical property analysis shows that 2D $MgMX_2Y_6$ possesses good absorption in the near-infrared, visible and ultraviolet regions, and holds great potential in multifunctional optoelectronic devices. The discussion in this report would be of great meaningful value for 2D $MgMX_2Y_6$.

Acknowledgements

This work was supported by the National Natural Science Foundation of China (Grant No. 61974049, 62222404, 61974050). L. Y. acknowledges National Key Research and Development Plan of China (Grant No. 2021YFB3601200). J. H. Y. acknowledges the Postdoctoral Fund of Hubei Province.

References

[1] Novoselov K S, Geim A K, Morozov S V, et al. Electric field effect in atomically thin carbon films. Science, 2004, 306, 666

[2] Akinwande D, Huyghebaert C, Wang C H, et al. Graphene and two-dimensional materials for silicon technology. Nature, 2019, 573, 507

[3] Yuan J H, Yu N N, Xue K H, et al. Ideal strength and elastic instability in single-layer 8-*Pmmn* borophene. RSC Adv, 2017, 7, 8654

[4] Yuan J H, Yu N N, Xue K H, et al. Stability, electronic and thermodynamic properties of aluminene from first-principles calculations. Appl Surf Sci, 2017, 409, 85

[5] Balendhran S, Walia S, Nili H, et al. Elemental analogues of graphene: Silicene, germanene, stanene, and phosphorene. Small, 2015, 11, 640

[6] Yuan P W, Zhang T, Sun J T, et al. Recent progress in 2D group-V elemental monolayers: Fabrications and properties. J Semicond, 2020, 41, 081003

[7] Wang Y X, Qiu G, Wang R X, et al. Field-effect transistors made from solution-grown two-dimensional tellurene. Nat Electron, 2018, 1, 228

[8] Liu Y, Duan X D, Huang Y, et al. Two-dimensional transistors beyond graphene and TMDCs. Chem Soc Rev, 2018, 47, 6388

[9] Tong L, Peng Z R, Lin R F, et al. 2D materials-based homogeneous transistor-memory architecture for neuromorphic hardware. Science, 2021, 373, 1353

[10] Morales-García Á, Calle-Vallejo F, Illas F. MXenes: New horizons in catalysis. ACS Catal, 2020, 10, 13487

[11] Wang L, Shi Y P, Liu M F, et al. Intercalated architecture of MA_2Z_4 family layered van der Waals materials with emerging topological, magnetic and superconducting properties. Nat Commun, 2021, 12, 2361

[12] Ding W J, Zhu J B, Wang Z, et al. Prediction of intrinsic two-dimensional ferroelectrics in In_2Se_3 and other III_2-VI_3 van der Waals materials. Nat Commun, 2017, 8, 14956

[13] Deng J, Deng D H, Bao X H. Robust catalysis on 2D materials encapsulating metals: Concept, application, and perspective. Adv Mater, 2017, 29, 1606967

[14] Lemme M C, Akinwande D, Huyghebaert C, et al. 2D materials for future heterogeneous electronics. Nat Commun, 2022, 13, 1392

[15] Tang K, Wang Y, Gong C H, et al. Electronic and photoelectronic memristors based on 2D materials. Adv Elect Mater, 2022, 8, 2101099

[16] Anichini C, Czepa W, Pakulski D, et al. Chemical sensing with 2D materials. Chem Soc Rev, 2018, 47, 4860
[17] Wu F, Tian H, Shen Y, et al. Vertical MoS_2 transistors with sub-1-nm gate lengths. Nature, 2022, 603, 259
[18] Li X F, Yu Z Q, Xiong X, et al. High-speed black phosphorus field-effect transistors approaching ballistic limit. Sci Adv, 2019, 5, eaau3194
[19] Wang Y C, Lv J, Zhu L, et al. CALYPSO: A method for crystal structure prediction. Comput Phys Commun, 2012, 183, 2063
[20] Glass C W, Oganov A R, Hansen N. USPEX—Evolutionary crystal structure prediction. Comput Phys Commun, 2006, 175, 713
[21] Yu W Y, Niu C Y, Zhu Z L, et al. Atomically thin binary V-V compound semiconductor: A first-principles study. J Mater Chem C, 2016, 4, 6581
[22] Jin X, Tao L, Zhang Y Y, et al. Intrinsically scale-free ferroelectricity in two-dimensional $M_2X_2Y_6$. Nano Res, 2022, 15, 3704
[23] Miao N H, Li W, Zhu L G, et al. Tunable phase transitions and high photovoltaic performance of two-dimensional $In_2Ge_2Te_6$ semiconductors. Nanoscale Horiz, 2020, 5, 1566
[24] Hao K R, Ma X Y, Lyu H Y, et al. The atlas of ferroicity in two-dimensional $MGeX_3$ family: Room-temperature ferromagnetic half metals and unexpected ferroelectricity and ferroelasticity. Nano Res, 2021, 14, 4732
[25] Hao K R, Ma X Y, Zhang Z, et al. Ferroelectric and room-temperature ferromagnetic semiconductors in the 2D $M_IM_{II}Ge_2X_6$ family: First-principles and machine learning investigations. J Phys Chem Lett, 2021, 12, 10040
[26] Nityananda R, Hohenberg P, Kohn W. Inhomogeneous electron gas. Reson, 2017, 22, 809
[27] Blöchl P E. Projector augmented-wave method. Phys Rev B, 1994, 50, 17953
[28] Kresse G, Joubert D. From ultrasoft pseudopotentials to the projector augmented-wave method. Phys Rev B, 1999, 59, 1758
[29] Kresse G, Furthmüller J. Efficiency of ab-initio total energy calculations for metals and semiconductors using a plane-wave basis set. Comput Mater Sci, 1996, 6, 15
[30] Kresse G, Furthmüller J. Efficient iterative schemes for *ab initio* total-energy calculations using a plane-wave basis set. Phys Rev B, 1996, 54, 11169
[31] Perdew J P, Burke K, Ernzerhof M. Generalized gradient approximation made simple. Phys Rev Lett, 1996, 77, 3865
[32] Xue K H, Yuan J H, Fonseca L R C, et al. Improved LDA-1/2 method for band structure calculations in covalent semiconductors. Comput Mater Sci, 2018, 153, 493
[33] Yuan J H, Chen Q, Fonseca L R C, et al. GGA-1/2 self-energy correction for accurate band structure calculations: The case of resistive switching oxides. J Phys Commun, 2018, 2, 105005
[34] Krukau A V, Vydrov O A, Izmaylov A F, et al. Influence of the exchange screening parameter on the performance of screened hybrid functionals. J Chem Phys, 2006, 125, 224106
[35] Togo A, Oba F, Tanaka I. First-principles calculations of the ferroelastic transition between rutile-type and $CaCl_2$-type SiO_2 at high pressures. Phys Rev B, 2008, 78, 134106
[36] Jin H, Tan X X, Wang T, et al. Discovery of two-dimensional multinary component photocatalysts accelerated by machine learning. J Phys Chem Lett, 2022, 13, 7228
[37] Kamal C, Ezawa M. Arsenene: Two-dimensional buckled and puckered honeycomb arsenic systems. Phys Rev B, 2015, 91, 085423
[38] Liu Z, Wang H D, Sun J Y, et al. Penta-Pt_2N_4: An ideal two-dimensional material for nanoelectronics. Nanoscale, 2018, 10, 16169
[39] Yuan J H, Song Y Q, Chen Q, et al. Single-layer planar penta-X_2N_4 (X = Ni, Pd and Pt) as direct-bandgap semiconductors from first principle calculations. Appl Surf Sci, 2019, 469, 456
[40] Born M, Huang K. Dynamical theory of crystal lattices. Oxford: Clarendon Press, 1954
[41] Tang W, Sanville E, Henkelman G. A grid-based Bader analysis algorithm without lattice bias. J Phys: Condens Matter, 2009, 21, 084204
[42] Liu F, Ming P B, Li J. *Ab initio* calculation of ideal strength and phonon instability of graphene under tension. Phys Rev B, 2007, 76, 064120
[43] Andrew R C, Mapasha R E, Ukpong A M, et al. Mechanical properties of graphene and boronitrene. Phys Rev B, 2012, 85, 125428
[44] Li J W, Medhekar N V, Shenoy V B. Bonding charge density and ultimate strength of monolayer transition metal dichalcogenides. J Phys Chem C, 2013, 117, 15842
[45] Li J, Zhou W H, Xu L L, et al. Revealing the weak Fermi level pinning effect of 2D semiconductor/2D metal contact: A case of monolayer $In_2Ge_2Te_6$ and its Janus structure $In_2Ge_2Te_3Se_3$. Mater Today Phys, 2022, 26, 100749
[46] Yuan J H, Zhang B, Song Y Q, et al. Planar penta-transition metal phosphide and arsenide as narrow-gap semiconductors with ultrahigh carrier mobility. J Mater Sci, 2019, 54, 7035

Junhui Yuan received the B.S./M.S. degree from Wuhan University of Technology, P. R. China, in 2013/2016 and the Ph.D. degree in Microelectronics and Solid-State Electronics, Huazhong University of Science and Technology, P.R. China, in 2020. He is currently a postdoctoral fellow in the School of Integrated Circuits, Huazhong University of Science and Technology. He is working on the theory research of Hafnia-based ferroelectricity. His research interests include modeling of volatile and non-volatile resistive switching, novel shell DFT-1/2 computational method and prediction of novel functional materials.

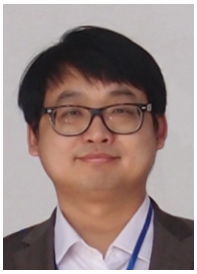

Kanhao Xue received the B.S. and M.S. degrees in electronic engineering from Tsinghua University, Beijing, China, and the Ph.D. degree in electrical engineering from the University of Colorado at Colorado Springs, USA, in 2010. Hs is now a professor at School of Integrated Circuits, Huazhong University of Science and Technology. He is working on first-principles calculations and novel methods on electronic band structure calculation in semiconductors. He has authored and co-authored more than 120 articles in international refereed journals.

Lei Ye received the B.S. and M.S. degrees from Hunan University, and the Ph.D. degree in electrical engineering from the Chinese University of Hongkong. He is now a professor at School of Integrated Circuits, Huazhong University of Science and Technology. He is working on 2D materials and 2D materials-based devices. He has authored and co-authored more than 70 articles in international refereed journals, including: Science, Nature communications.